



Contents lists available at ScienceDirect

## Arabian Journal of Chemistry

journal homepage: [www.ksu.edu.sa](http://www.ksu.edu.sa)

# Bimetallic FeCo metal–organic framework based cascade reaction system: Enhanced peroxidase activity for antibacterial performance

Siyuan Zhang<sup>a,1</sup>, Wenbo Wu<sup>a,1</sup>, Ya Li<sup>a</sup>, Dongxin Wang<sup>a,b</sup>, Xiangjun Li<sup>c</sup>, Jisheng Nie<sup>a,b,\*</sup>, Hong Cui<sup>a,b,\*</sup>

<sup>a</sup> School of Public Health, Shanxi Medical University, 56 Xinjian South Road, Taiyuan 030001, China

<sup>b</sup> MOE Key Laboratory of Coal Environmental Pathogenicity and Prevention, Shanxi Medical University, 56 Xinjian South Road, Taiyuan 030001, China

<sup>c</sup> School of Chemical Sciences, University of Chinese Academy of Sciences, 19A Yuquan Road, Beijing 100049, China

## ARTICLE INFO

## Keywords:

Nanozymes  
Bimetallic metal–organic frameworks (MOFs)  
Glucose  
Cascade reaction  
Antibacterial properties

## ABSTRACT

Metal-organic frameworks (MOFs), as a peroxidase (POD), can catalyze the conversion of H<sub>2</sub>O<sub>2</sub> to reactive oxygen species (ROS) for antibacterial application. To achieve strong antibacterial activity, it is necessary to improve the enzyme-like activity of MOFs. In this study, Fe<sub>x</sub>CoMOF was synthesized by incorporating Co(II) to improve the electron transfer of Fe(III)/Fe(II), which enhanced its redox capacity as a nanozyme and further promoted the generation of hydroxyl radical ( $\cdot$ OH), exhibiting higher POD activity. Doping with different amounts of Co(II) altered the particle size, specific surface area, and surface defects of Fe<sub>x</sub>CoMOF, thus exhibiting differential enzyme-like activities. Additionally, a glucose-responsive enzyme cascade reaction system based on Fe<sub>4</sub>CoMOF/glucose oxidase (GOx) was established. In the presence of glucose, the *in situ*-generated substrate H<sub>2</sub>O<sub>2</sub> was in contact with the catalytic site and the generated gluconic acid enabled Fe<sub>4</sub>CoMOF to maintain maximum enzyme activity under physiological pH conditions, avoiding damage caused by the use of exogenous high concentrations of H<sub>2</sub>O<sub>2</sub>. In the *in vitro* antibacterial experiment, the minimum inhibitory concentration (MIC) of Fe<sub>4</sub>CoMOF/GOx was 10 μg mL<sup>-1</sup> for *Escherichia coli* (*E. coli*) and 5 μg mL<sup>-1</sup> for *Staphylococcus aureus* (*S. aureus*) (~10<sup>8</sup> CFU mL<sup>-1</sup>). The increase in enzyme activity resulted in a considerable reduction in the dose of the antibacterial agent, which was conducive to improving bio-safety. The *in vivo* experiment in mice demonstrated that the glucose-responsive Fe<sub>4</sub>CoMOF-based cascade reaction system had excellent antibacterial properties and remarkably promoted wound healing. The antibacterial agent based on bimetallic MOF developed in this work provides a new idea for cascade catalytic antibacterial therapy and will have remarkable application prospects in biomaterials and nanomedicine.

## 1. Introduction

Bacterial infections, such as wound inflammation, bacterial pneumonia, and urinary tract infection, are serious threats to human health and are major problems in biomedicine (Chen et al., 2018; Jones et al., 2008; Koo et al., 2017). Antibiotics have been a successful strategy for treating bacterial diseases (Matlock et al., 2021; Ye et al., 2022), but the consequent problem of bacterial antibiotic resistance has become one of the major threats to public health (Yang et al., 2022). Therefore, the development of new antibacterial agents based on non-antibiotic antimicrobial therapy has become a hot research topic in the biomedicine field (Kong and Yang, 2021; Xi et al., 2019). Nanozymes are

nanomaterials with similar activity to that of natural enzymes, but they overcome some of the inherent shortcomings of natural enzymes and have the advantages of high stability, low cost, good biocompatibility, and unique catalytic activity (Mei et al., 2021; Zhang et al., 2020). They also have unique physical and chemical properties that can be used to regulate the size, composition, structure, and surface modification of nanomaterials, thereby modulating enzyme activity. With the development of nanozymes and the elucidation of their catalytic mechanisms, nanozymes have attracted increasing attention in the biomedicine field (Li et al., 2021b; Xiong et al., 2019). Nanozymes have the ability to regulate the level of ROS free radicals, especially the oxidase (OXD)-like and peroxidase (POD)-like activities of nanozymes, which can catalyze

\* Corresponding authors.

E-mail addresses: [niejisheng@sxmu.edu.cn](mailto:niejisheng@sxmu.edu.cn) (J. Nie), [cuihong19872007@126.com](mailto:cuihong19872007@126.com) (H. Cui).

<sup>1</sup> co-first authors.

the generation of a free radical storm from  $O_2$  or  $H_2O_2$  in a short period of time, thus conferring antimicrobial functions to nanozymes (Huang et al., 2019).

Metal-organic frameworks (MOFs) are characterized by the uniform distribution of unsaturated metal active sites, porous skeleton, adjustable pore size, etc., so that the substrate has a large number of opportunities to approach the catalytic site, which is conducive to significantly improve the catalytic performance and generate more ROS to achieve a stronger antibacterial effect, and thus have received extensive attention in the field of antibacterial agents (Alavijeh et al., 2018; Maleki et al., 2020). Improving the enzyme activity of MOFs and producing more ROS is the key to enhance their antibacterial effect. Metal nodes are considered to be the center of catalytic activity of MOFs-based nanozymes, so adjusting the metal nodes of MOFs is considered to be a feasible strategy to modulate the catalytic activity, where promoting to the multivalent redox cycling ability of the metal nodes is crucial (Huang et al., 2022). Bimetallic MOFs integrate two metal ions into the same structure, forming a special type of MOFs (Chen et al., 2020). Compared with mono-metallic MOFs, bimetallic MOFs can regulate the processes of electron acceptance and electron donation by adjusting the types and ratios of the two metal ions to produce different catalytically active sites and adsorption sites, which can play a synergistic role in obtaining better catalytic activity (Liang et al., 2021; Wang et al., 2020). Functionalization of FeMOF with Co sites enhanced the catalytic activity for the degradation of organic pollutants (Wen et al., 2021). It has been shown that NiFe<sub>2</sub>MOF has a tendency to transfer electrons from Ni<sup>2+</sup> to Fe<sup>3+</sup>, and the resulting Fe<sup>2+</sup> can decompose H<sub>2</sub>O<sub>2</sub> to produce hydroxyl radical ( $\cdot OH$ ) via a Fenton-like reaction, which exhibits enhanced POD-like activity (Zhao et al., 2021b). Another Fe-Ni bimetallic MOF has also been developed for the detection of H<sub>2</sub>O<sub>2</sub> and glucose (Glu) based on its POD-like activity, which is enhanced by a dual mechanism of electron transfer and  $\cdot OH$  formation (Mu et al., 2022). Currently, several bimetallic MOF systems have been developed for antibacterial or wound healing purposes. For example, MOF(Fe-Cu)/glucose oxidase (GOx)-polyacrylamide (PAM) gel has been reported to accelerate wound healing through synergistic antibacterial and inflammatory modulation (Tian et al., 2023). Another article reported that the introduction of Zn into MIL-88B-Fe/Zn could also regulate the electronic structure of Fe, thereby accelerating the catalytic kinetics of its POD-like activity, showing satisfactory antibacterial effects both *in vitro* and *in vivo* (Shi et al., 2023). The application of bimetallic MOF nanozymes based on multi-active site engineering in antibacterial applications is yet to be vigorously developed.

To improve the antibacterial effect of POD-like nanozymes, high H<sub>2</sub>O<sub>2</sub> levels are typically required, however, these high levels can severely damage normal tissues (Yang et al., 2020). Nanozyme-based cascade reaction system provides an opportunity to solve this problem by integrating nanozymes and enzymatic reactions into one entity, wherein the product of the enzymatic reaction serve as the substrate of the nanozyme, increasing the local concentration of the substrate and shortening the distance between the reaction site and the substrate, thus improving catalytic performance (Ma et al., 2019; Zhang et al., 2019). Moreover, the enzymatic reaction can reduce the pH of the system to the value at which the nanozyme exerts optimal enzyme activity. The high porosity and specific surface area of MOFs endow them a competitive advantage for efficient encapsulation other enzymes to construct cascade reaction systems (Li et al., 2020; Liu et al., 2019; Wu et al., 2015).

Herein, we successfully synthesized several bimetallic MOFs with Fe (III) and Co(II) as metal centers. The physical and chemical properties of Fe<sub>x</sub>CoMOF, such as particle size, specific surface area, and surface defects, were well improved by doping with different amounts of Co(II). Meanwhile, the import of Co(II) accelerated electron transport between Fe(III) and Fe(II), thus promoting the formation of  $\cdot OH$  and enhancing the POD-like activity. In addition, a Fe<sub>4</sub>CoMOF-based cascade reaction system with dual enzyme activity was constructed by loading GOx onto

Fe<sub>4</sub>CoMOF through physisorption, further improving the catalytic performance and practical antibacterial applicability (Scheme 1). The Glu-responsive Fe<sub>4</sub>CoMOF/GOx showed outstanding antibacterial activity against *E. coli* and *S. aureus* ( $\sim 10^8$  CFU mL<sup>-1</sup>) with low minimal inhibitory concentration (MIC), and significant healing and excellent antimicrobial performance of mouse skin infected wounds were observed in *in vivo* antibacterial assays.

## 2. Materials and methods

### 2.1. Materials

Iron chloride hexahydrate (FeCl<sub>3</sub>·6H<sub>2</sub>O), cobalt nitrate hexahydrate (Co(NO<sub>3</sub>)<sub>2</sub>·6H<sub>2</sub>O), 3,3',5,5'-tetramethylbenzidine (TMB, 98 %), H<sub>2</sub>O<sub>2</sub> (30 %), glucose (Glu), and terephthalic acid (TA, 99 %) were obtained from Aladdin Chemistry Co., Ltd. (Shanghai, China). Absolute ethanol (99.7 %) and N, N-Dimethylformamide (DMF, 99.5 %) were purchased from Shanghai Roche Pharmaceutical Co., Ltd. (Shanghai, China). GOx was obtained from Sangon Biotechnology, Inc. (Shanghai, China). Other reagents that were not labeled were analytically pure. All chemicals were used as received without further purification.

### 2.2. Preparation of Fe<sub>x</sub>CoMOFs and Fe<sub>x</sub>CoMOFs/GOx

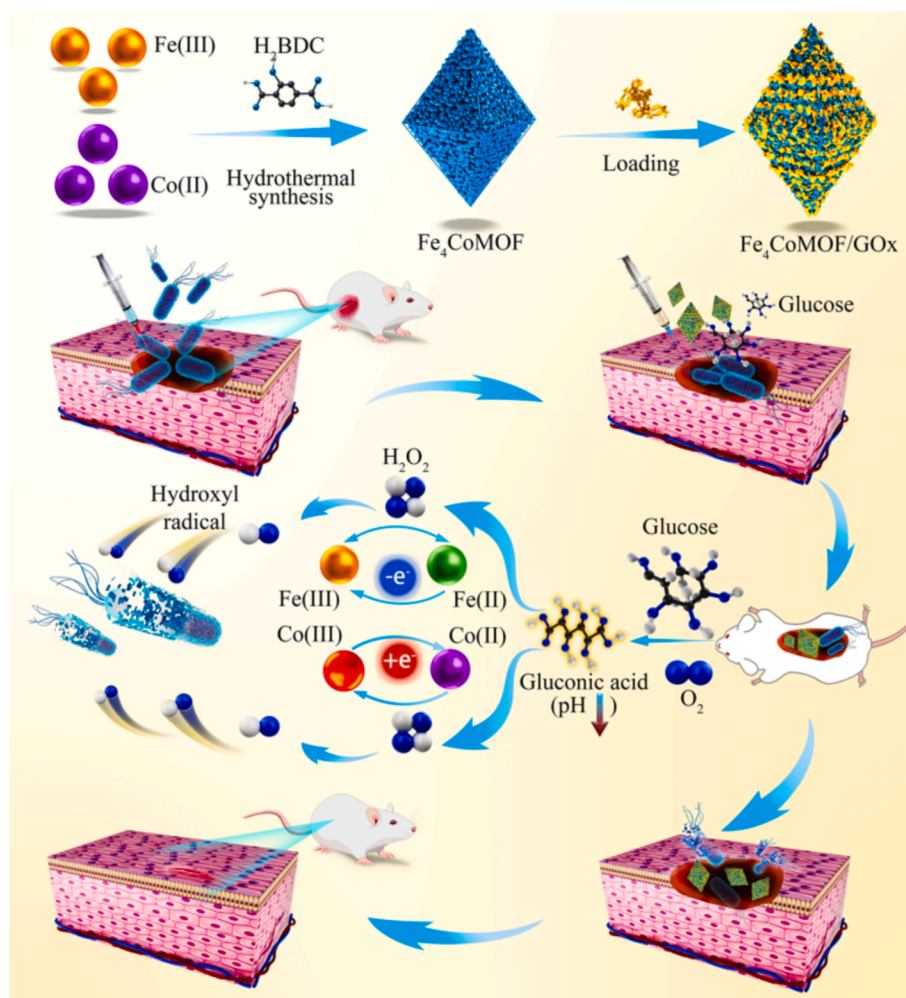
Fe<sub>4</sub>CoMOF was synthesized using a simple solvothermal method. Specifically, 0.86 g FeCl<sub>3</sub>·6H<sub>2</sub>O, 0.23 g Co(NO<sub>3</sub>)<sub>2</sub>·6H<sub>2</sub>O, and 0.66 g TA were dissolved in 80 mL breaker containing DMF, magnetically stirred for 3 h, and transferred to a 150 mL polytetrafluoron-lined autoclave at 110°C for 20 h. After the reaction, the material was cooled to room temperature, washed thrice by centrifugation with DMF and alcohol, respectively, and dried overnight at 60°C in a vacuum oven. In addition, Fe<sub>x</sub>CoMOFs with other molar ratios (x = 5 and 3) and MOFs containing only Fe or Co were synthesized using the same method. Then, 5 mg Fe<sub>x</sub>CoMOF was dissolved in 5 mL of ultrapure water, followed by the addition of 2.5 mg of GOx, slowly stirred at room temperature for 12 h, and washed thrice with ultrapure water to obtain Fe<sub>x</sub>CoMOF/GOx, which was stored in a refrigerator at 4°C for future use.

### 2.3. POD-like activity and steady-state kinetic analyses of Fe<sub>x</sub>CoMOFs

Using TMB as a substrate, the POD-like activity of Fe<sub>x</sub>CoMOFs in the presence of H<sub>2</sub>O<sub>2</sub> was studied. TMB (1.2 mM) and H<sub>2</sub>O<sub>2</sub> (10 mM) were first added to HAC-NaAc buffer (0.1 M, pH 4.0), and then 25 μg mL<sup>-1</sup> Fe<sub>x</sub>CoMOFs was added to the solution. The A<sub>652nm</sub> was measured using a multimode reader after incubation at room temperature for 3 min. The steady-state kinetic analysis was performed by monitoring the change in A<sub>652nm</sub> using a series of H<sub>2</sub>O<sub>2</sub> concentrations ranging from 1 to 100 mM in an HAC-NaAc buffer (0.1 M, pH 4.0) containing 50 μg mL<sup>-1</sup> Fe<sub>x</sub>CoMOFs and 0.9 mM TMB. Similar to that using H<sub>2</sub>O<sub>2</sub>, the kinetic experiment using TMB as the substrate involves maintaining the concentration of H<sub>2</sub>O<sub>2</sub> at 10 mM and monitoring the changes in absorbance when the concentration of TMB is in the range of 0.1 to 1.5 mM. The kinetic parameters were calculated using the Lineweaver-Burk equation  $1/v = K_m/(V_{max} [S]) + 1/V_{max}$ , where  $v$  and  $V_{max}$  are the initial and maximum reaction velocities, respectively,  $[S]$  is the substrate concentration, and  $K_m$  is the Michaelis constant.

### 2.4. CV measurements

1 mg of FeMOF, CoMOF, and various molar ratios of Fe<sub>x</sub>CoMOFs were dispersed in 1 mL ultra-pure water containing 2 μL nafion and mixed ultrasonically. A glassy carbon electrode (GCE) with 8 μL of the material solution, a platinum wire electrode, and a saturated calomel electrode were used to perform CV tests in a pre-deoxygenated HAC-NaAc buffer (pH 4.0, 0.1 M) or a buffer containing a certain concentration of H<sub>2</sub>O<sub>2</sub> with the scan rate at 10 mV s<sup>-1</sup>.



**Scheme 1.** Schematic illustration of the synthesis and antibacterial application of  $\text{Fe}_4\text{CoMOF/GOx}$ .

### 2.5. Detection of $\cdot\text{OH}$

The fluorescence spectra of  $\text{Fe}_x\text{CoMOFs}$  with different molar ratios were determined in the presence of TA (1 mM) and  $\text{H}_2\text{O}_2$  (10 mM). For the cascade reaction, various reaction systems were incubated with TA (0.5 mM) in PBS buffer (pH 7.4, 0.5 mM) for 12 h, and fluorescence spectra were recorded. For ESR measurement, DMPO was employed as a trapping probe to demonstrate the presence of  $\cdot\text{OH}$ . In HAC-NaAc buffer (pH 4.0, 0.1 M),  $1 \text{ mg mL}^{-1}$   $\text{Fe}_x\text{CoMOFs}$  and 10 mM  $\text{H}_2\text{O}_2$  were reacted at room temperature for 10 min, and 100  $\mu\text{L}$  of the reaction solution was added to 100  $\mu\text{L}$  of DMPO solution at a concentration of 100 mM to be mixed well and put into sample tubes after capillary loading and sealing, and then put into a machine for testing and collecting data. In addition, the  $\cdot\text{OH}$  produced by the reaction of  $1 \text{ mg mL}^{-1}$   $\text{Fe}_4\text{CoMOF}$  and 10 mM  $\text{H}_2\text{O}_2$  for 3, 5, 8 and 10 min was quantified using ESR.

### 2.6. Construction of cascade system based on $\text{Fe}_4\text{CoMOF/GOx}$

The cascade reaction system comprised 1.2 mM TMB, 10 mM Glu, 20  $\mu\text{g mL}^{-1}$   $\text{Fe}_4\text{CoMOF/GOx}$ , and PBS buffer (pH 7.4, 0.5 mM) (designated as (V) Glu +  $\text{Fe}_4\text{CoMOF/GOx}$ ). The color change of the system was photographed, and UV-vis spectra were recorded using a multimode reader after incubation at  $37^\circ\text{C}$  for 4 h. Meanwhile, the color and spectral changes in the control group (I) PBS, (II) Glu, (III) Glu + GOx, (IV) Glu +  $\text{Fe}_4\text{CoMOF}$  and (VI)  $\text{Fe}_4\text{CoMOF/GOx}$  were measured. If there is no further clarification, this pattern will be followed for all groups in subsequent experiments. Methyl red (0.001 %) was used to determine

the pH of the solution after incubation of each group to confirm the production of gluconic acid. The effect of the concentration of PBS buffer, incubation time and Glu concentration were also determined.

### 2.7. Cytotoxicity experiments

Cell Counting Kit-8 (CCK-8) was used for cytotoxicity tests. Mouse fibroblast L929 cells were selected to assess cell viability and evaluate the biocompatibility of the material. L929 cells were cultured in a standard DMEM medium containing 10 % fetal bovine serum. The cells were first incubated in a humidified incubator ( $37^\circ\text{C}$ , 5 %  $\text{CO}_2$ ) for 24 h in 96-well plates (approximately 5000 cells per well, 10 wells per concentration). After washing with PBS (10 mM, pH 7.4), various concentrations of  $\text{Fe}_4\text{CoMOF}$  (0, 5, 10, 25, 40, and 50  $\mu\text{g mL}^{-1}$ ) were added to the wells and incubated for another 24 h; then, 10  $\mu\text{L}$  of the CCK-8 solution was added to each well and incubated for another 0.5 h. Finally, the absorbance at 450 nm of each well was measured using a microplate reader. The cells without  $\text{Fe}_4\text{CoMOF}$  were used as controls to calculate the cell viability relative to that of the control group. The results represent the average of values from three independent experiments.

### 2.8. In vitro antibacterial experiments

The bacterial diluent ( $10^8$  CFU  $\text{mL}^{-1}$ ) treated in the six groups was shaken continuously at 200 rpm and  $37^\circ\text{C}$  for 5 h, and the concentration of Glu was 10 mM and that of  $\text{Fe}_4\text{CoMOF/GOx}$  was  $10 \mu\text{g mL}^{-1}$ . For the plate coating method, the prepared bacterial solution was treated with

the same groups, and then 100  $\mu\text{L}$  of treated bacterial solution was separately dispersed on a solid medium and incubated at 37  $^{\circ}\text{C}$  for 12 h. Bacteria in the group I and V were collected via centrifugation at 5000 rpm for 3 min, fixed in 2.5 % glutaraldehyde at 4  $^{\circ}\text{C}$  for 16 h, dehydrated, and serially dried with an ethanol solution of various concentrations (10, 30, 50, 70, 90 %) for 10 min each time. The bacterial morphology was examined using SEM. To identify live and dead bacteria, fluorescence microscopic images of bacteria in the six treatment groups were obtained using the Calcein-AM/PI staining method. The bacterial solutions were incubated with a mixture of Calcein-AM (2  $\mu\text{M}$ ) and PI (1.6  $\mu\text{M}$ ) at 37  $^{\circ}\text{C}$  for 30 min and then washed with sterile PBS thrice and observed under a fluorescence microscope. Qualitative assessment of intracellular ROS in *E. coli* and *S. aureus* after each group of treatments was performed using the DCFH-DA probe.

### 2.9. In vivo mice wound model

The experimental mice (BALB/c, 6–8 weeks old) were purchased from the Experimental Animal Center of the Shanxi Medical University (Approval No. 2022–046). All animals were approved by the Experimental Animal Welfare Ethics Committee of Shanxi Medical University and raised in accordance with Laboratory animal – Guideline for the ethical review of the animal welfare of China (GB/T 35892–2018). After anesthetizing the mice with 5 % chloral hydrate, a wound with  $d \approx 10$  mm was surgically created on the backs of mice, and the injuries were infected with 20  $\mu\text{L}$  of an *E. coli* suspension to establish the wound infection model. The mice were randomly divided into six groups (five in each group) and treated with 20  $\mu\text{L}$  various groups. The concentrations of Glu and  $\text{Fe}_4\text{CoMOF}/\text{GOx}$  were 10 mM and 10  $\mu\text{g mL}^{-1}$ , respectively. The wounds of each group of mice were photographed every alternate day, and the weights of mice were recorded. Bacterial samples from wounds of each group were collected after 7 days and dispersed into 1 mL of physiological saline, 100  $\mu\text{L}$  of which was coated in Petri dishes and incubated at 37  $^{\circ}\text{C}$  for 24 h to evaluate the *in vivo* antibacterial effect of  $\text{Fe}_4\text{CoMOF}/\text{GOx} + \text{Glu}$  by plate colony counting. After 8 days of

treatment, the mice were sacrificed. Wound tissues from each group were collected and fixed with paraformaldehyde, and paraffin sections were analyzed using hematoxylin and eosin (H&E) staining and immunohistochemical staining analyses.

### 2.10. Statistical analysis

All data were shown as means  $\pm$  standard deviation (S.D). GraphPad Prism 9 and Origin 2019 were used for experimental data analysis and graphing. The comparison among multiple groups was used by one-way ANOVA.  $P < 0.05$  was denoted as statistically significant: (\*) for  $p < 0.05$ , (\*\*) for  $p < 0.01$ , (\*\*\*) for  $p < 0.001$ , and (\*\*\*\*) for  $p < 0.0001$ .

## 3. Results and discussion

### 3.1. Characterization of $\text{Fe}_x\text{CoMOFs}$

SEM and TEM were used to investigate the morphology of the MOFs synthesized with various molar ratios of Fe(III) and Co(II). A regular octahedral shape appeared when the content of doped Co(II) varied from 1:0 to 3:1, but the octahedral size and surface morphology were different (Fig. 1a–d). The FeMOF octahedron had a wrinkled, rough surface, whereas the  $\text{Fe}_5\text{CoMOF}$  had a slightly gauzy texture, approximately 1  $\mu\text{m}$  in size. When Co(II) content was increased to 4:1 and 3:1, small nanoparticles appeared on the cover of the octahedron, and the particle size was reduced to approximately 250 and 500 nm, respectively. The surface roughness might be related to structural defects (Reddy et al., 2022), which might be more conducive to the exposure of active catalytic sites and have a positive impact on the catalytic activity of nanozymes. However, when Fe(III) was entirely replaced by Co(II), the morphology of the MOF ultimately evolved, showing cuboid clusters, and the surface was smooth and defect-free (Fig. 1e). Thus, varying amounts of Co(II) doping had different degrees of influence on the shape, particle size, and surface roughness of the material; similar results have been reported in previous studies on bimetallic MOFs (Liang

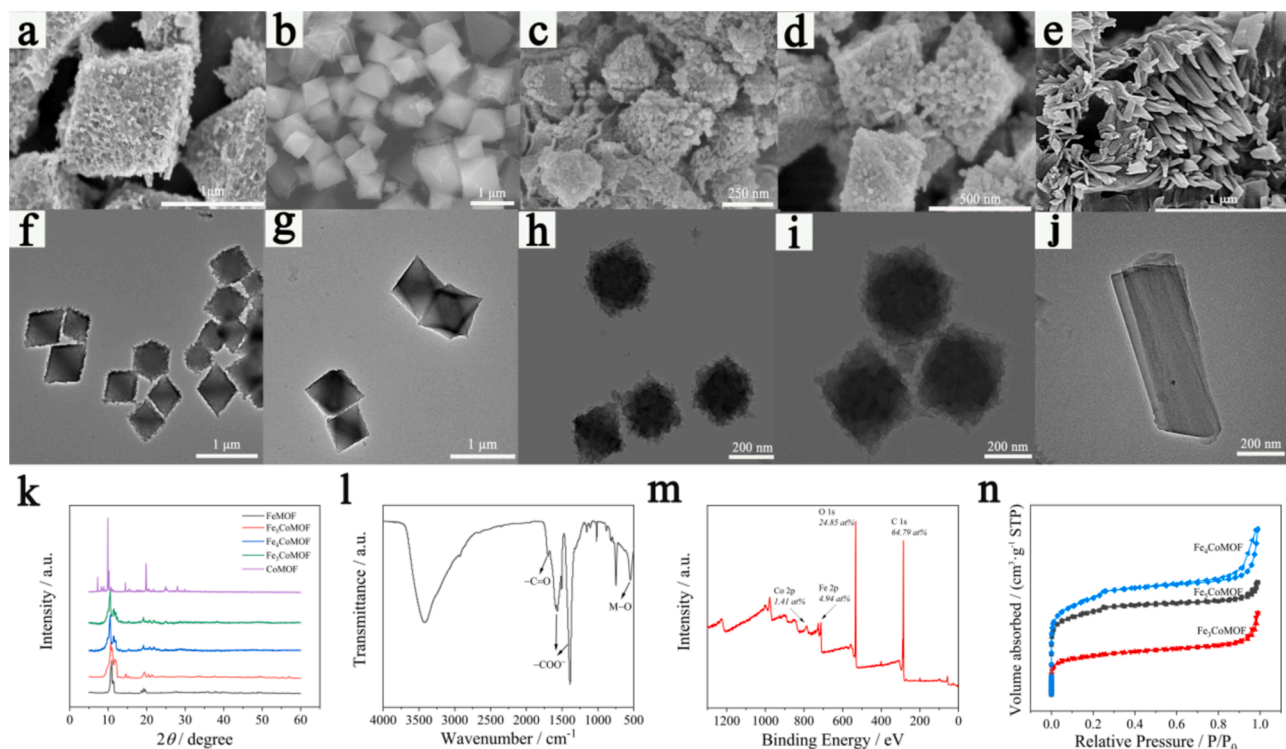


**Fig. 1.** SEM and TEM images of (a, f) FeMOF; (b, g)  $\text{Fe}_5\text{CoMOF}$ ; (c, h)  $\text{Fe}_4\text{CoMOF}$ ; (d, i)  $\text{Fe}_3\text{CoMOF}$ ; (e, j) CoMOF. (k) XRD patterns of FeMOF,  $\text{Fe}_5\text{CoMOF}$ ,  $\text{Fe}_4\text{CoMOF}$ ,  $\text{Fe}_3\text{CoMOF}$  and CoMOF. (l) FT-IR spectra of  $\text{Fe}_4\text{CoMOF}$ . (m) XPS full spectrum of  $\text{Fe}_4\text{CoMOF}$ . (n)  $\text{N}_2$  adsorption–desorption isotherms of  $\text{Fe}_x\text{CoMOF}$ .

et al., 2021; Wang et al., 2022a). The TEM images (Fig. 1f-j) also showed similar results, further confirming the successful synthesis of  $\text{Fe}_x\text{CoMOFs}$ .

The structural evolution of MOFs synthesized via Co doping was characterized using XRD, and the patterns were displayed in Fig. 1k.  $\text{FeMOF}$  and  $\text{Fe}_x\text{CoMOF}$  showed almost identical Bragg diffraction peaks, consistent with the results of previous studies (Liang et al., 2021; Wang et al., 2014), indicating that the bimetallic MOF material had the same structure as the  $\text{FeMOF}$  skeleton.  $\text{CoMOF}$  showed a completely different XRD pattern from that of  $\text{FeMOF}$  and  $\text{Fe}_x\text{CoMOFs}$ . All the above-mentioned XRD results were consistent with the different morphologies of several materials observed in SEM and TEM results. The defective structure formed with different doping contents might have a positive effect on the generation of  $\cdot\text{OH}$  by the contact between  $\text{H}_2\text{O}_2$  and the active catalytic site during the Fenton-like catalytic reaction.

For FT-IR analysis of  $\text{Fe}_4\text{CoMOF}$ , the results are shown in Fig. 1l. The characteristic peaks that appeared at approximately 1387 and 1570  $\text{cm}^{-1}$  were ascribed to the symmetric and asymmetric stretching vibrations of  $-\text{COO}^-$  (Wu et al., 2020), respectively, combined with the stretching vibration peak of  $-\text{C}=\text{O}$  at 1700  $\text{cm}^{-1}$  indicated the presence of TA ligands in the MOF. The band at approximately 549  $\text{cm}^{-1}$  was attributed to the  $\text{Fe}-\text{O}$  bending vibration (Jiang et al., 2024). In comparison, the weak peak at 623  $\text{cm}^{-1}$  originated from the  $\text{Co}-\text{O}$  bending vibration, indicating the formation of a bimetallic center in the  $\text{Fe}_4\text{CoMOF}$ .

The surface elemental composition of  $\text{Fe}_4\text{CoMOF}$  was studied using XPS. As shown in Fig. 1m, the peaks of C 1s, O 1s, Fe 2p, and Co 2p appeared in the survey XPS spectrum. In the high-resolution XPS spectra (Fig. S1) of C 1s, three peaks appeared at 288.7, 286.3, and 284.7 eV, corresponding to  $\text{C}=\text{O}$ ,  $\text{C}-\text{O}$ , and  $\text{C}-\text{C}$  bonds, respectively. For the O 1s spectrum, three peaks with binding energies of 533.4, 531.9, and 530.5 eV were attributed to  $\text{C}-\text{OH}$ ,  $\text{O}-\text{C}=\text{O}$ , and  $\text{M}-\text{O}$ , respectively. The C and O components derived from the TA ligand and  $\text{M}-\text{O}$  were produced by  $\text{Fe(III)}$  and  $\text{Co(II)}$  in coordination with TA. The peaks of Fe 2p

spectrum at 711.59 and 724.47 eV were attributed to  $\text{Fe(II)} 2p_{3/2}$  and  $\text{Fe(II)} 2p_{1/2}$ , and the peaks at 713.68 and 725.61 eV were assigned to  $\text{Fe(III)} 2p_{3/2}$  and  $\text{Fe(III)} 2p_{1/2}$ , which suggested that both  $\text{Fe(II)}$  and  $\text{Fe(III)}$  states were present in the synthesized bimetallic MOF (Tian et al., 2023). Peaks of  $\text{Co(II)}$  and  $\text{Co(III)}$  were observed for both  $\text{Co} 2p_{3/2}$  and  $\text{Co} 2p_{1/2}$  at 783.67, 781.16 eV and 794, 791.8 eV, respectively, and the peak intensities were weak, which indicated that the Co content was low. The successful synthesis of  $\text{Fe}_4\text{CoMOF}$  was also confirmed by the relative content ratio of  $\text{Fe(III)}$  and  $\text{Co(II)}$  approaching approximately 4:1.

The influence of the molar ratio of different metals on the BET surface area and pore size of  $\text{Fe}_x\text{CoMOFs}$  was investigated by  $\text{N}_2$  adsorption-desorption analysis (Fig. 1n). The adsorption and desorption curves indicate the existence of microporous structures. The BET surface area of  $\text{Fe}_5\text{CoMOF}$ ,  $\text{Fe}_4\text{CoMOF}$  and  $\text{Fe}_3\text{CoMOF}$  were 224, 565 and 478  $\text{m}^2 \text{g}^{-1}$ , respectively. At the same time, the pore size and pore volume also changed, which might be related to the defects formed on the surface of the material during the competitive coordination of the two metal ions, resulting in larger free volume in the pore channels of MOFs materials. The free volume caused by the defect site directly led to a larger specific surface area and higher porosity of the material. The large specific surface area facilitated the adsorption of substrate molecules at the catalytic sites and the formation of complexes with other substances. These results indicated that doping of different amounts of Co affects the porous structure of MOF.

### 3.2. POD-like activity of $\text{Fe}_x\text{CoMOFs}$

The effects of various molar ratios of  $\text{Fe(III)}$  and  $\text{Co(II)}$  on POD activity were investigated. As shown in Fig. 2a, in the presence of  $\text{FeMOF}$  or  $\text{Fe}_x\text{CoMOFs}$  and the two substrates TMB and  $\text{H}_2\text{O}_2$ , the color of the solutions changed from colorless to blue, with a characteristic absorption peak at 652 nm, which originated from the oxidized TMB (oxTMB).  $\text{CoMOF}$  showed a very weak absorption peak, which could only be enhanced to a certain extent with increasing temperature. These results

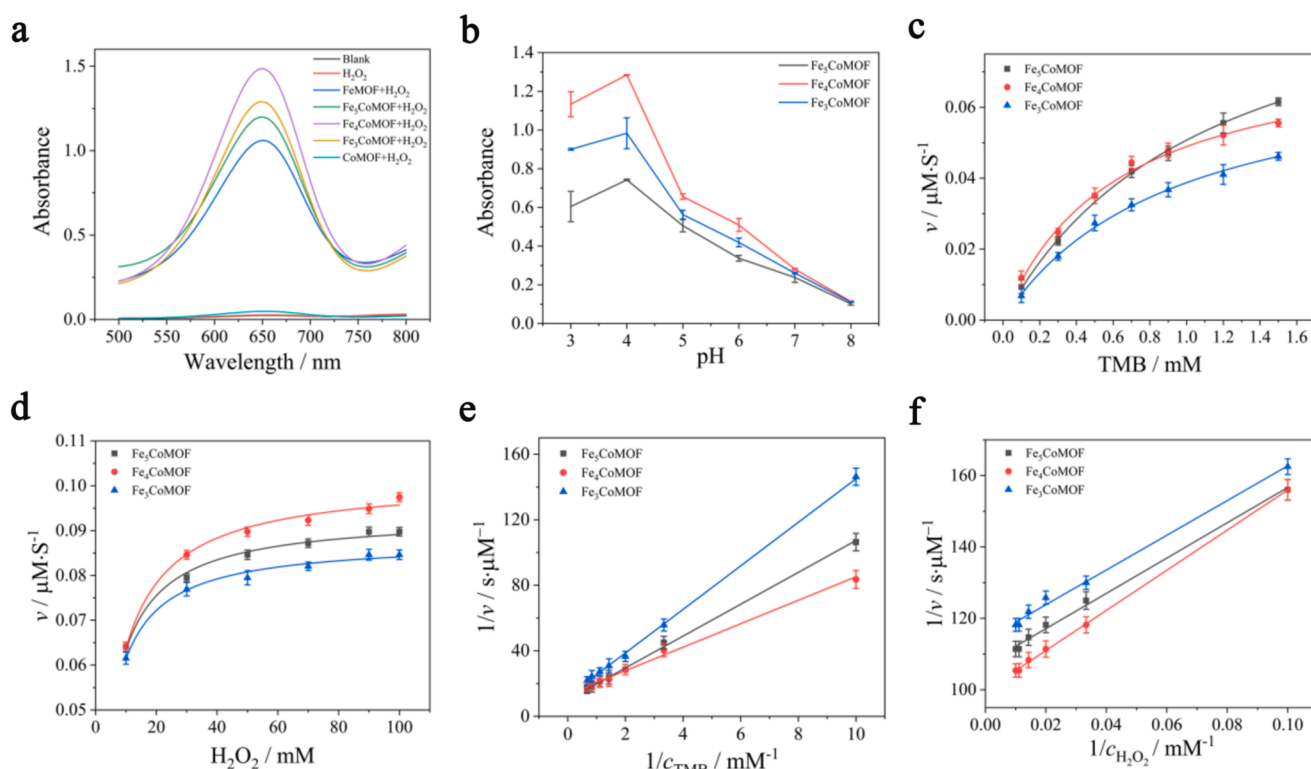


**Fig. 2.** (a) The absorption spectra of the various reaction systems in the presence of TMB. (b) Influence of pH on the POD-like activity of  $\text{Fe}_x\text{CoMOFs}$  in the presence of  $\text{H}_2\text{O}_2$  and TMB. (c), (d), (e), (f) Michaelis-Menten kinetics and Lineweaver-Burk plotting of  $\text{Fe}_x\text{CoMOFs}$  with TMB and  $\text{H}_2\text{O}_2$  as the substrate.

suggested that FeMOF had a certain POD-like activity, as reported in many studies, and the enzyme catalytic activity of CoMOF was fragile. After the introduction of Co(II) into FeMOF, the enzyme-like activity of bimetallic MOF improved tremendously, which might be related to the improved electron transfer efficiency (Tian et al., 2023). Moreover, different proportions of Co doping also affected the catalytic activity of enzymes, and the enzyme catalytic activity was highest for Fe<sub>4</sub>CoMOF.

The three catalysts with varying molar ratios exhibited the highest activities at pH 4.0 (Fig. 2b). To determine the POD-like catalytic activity of Fe<sub>x</sub>CoMOFs, the steady-state kinetic parameters  $K_m$  and  $V_{max}$  were calculated from the Michaelis-Menten curves (Fig. 2c-f) and are summarized in Table 1. The  $K_m$  values of the three Fe<sub>x</sub>CoMOFs with H<sub>2</sub>O<sub>2</sub> as the substrate were lower than those of the MOFs with TMB as the substrate, indicating that the affinity of Fe<sub>x</sub>CoMOFs for H<sub>2</sub>O<sub>2</sub> was higher than that of TMB. In this catalytic process, the addition of various Co(II) ions might lead to the production of different ·OH radicals by influencing the electron transfer of Fe(III), resulting in various enzyme activities. The  $K_m$  value of Fe<sub>4</sub>CoMOF was the lowest, indicating that it had the highest affinity for H<sub>2</sub>O<sub>2</sub>. The different affinities for H<sub>2</sub>O<sub>2</sub> are related to the structure and morphology of different Fe<sub>x</sub>CoMOFs, which expose different active sites. In addition, the various specific surface areas of these three types of Fe<sub>x</sub>CoMOFs led to different adsorption capacities for H<sub>2</sub>O<sub>2</sub>. The steady-state kinetic parameters were also compared with other MOF-based POD-like catalysts including FeMOF, CoMOF and bimetallic MOF, and the results are summarized in Table S1, in which the Fe<sub>4</sub>CoMOF in this paper exhibited lower  $K_m$  and higher  $V_{max}$ , indicating its excellent substrate affinity and catalytic activity.

The destiny of the catalyst was examined after MOF exerted its POD-like activity to catalyze H<sub>2</sub>O<sub>2</sub>. SEM (Fig. S2a and Fig. S2b) results showed that Fe<sub>4</sub>CoMOF still exhibited an octahedral morphology after the reaction with H<sub>2</sub>O<sub>2</sub>, indicating that Fe<sub>4</sub>CoMOF had a very good stability, which is in agreement with the XRD results (Fig. S2c). The FT-IR (Fig. S2d) spectrum had no obvious change after the reaction between Fe<sub>4</sub>CoMOF and H<sub>2</sub>O<sub>2</sub>, which suggested that there was no destruction of the groups of Fe<sub>4</sub>CoMOF after the catalytic reaction. After catalyzing H<sub>2</sub>O<sub>2</sub>, the ratio of Fe(II) to Fe(III) was slightly increased in the XPS spectra (Fig. S1), while the ratio of Co(III) to Co(II) was significantly increased, which was attributed to the fact that Fe acted as a catalytic center involved in the reaction of generating free radicals and their intermediates from H<sub>2</sub>O<sub>2</sub>, which induced a change of the valence state of Fe in the process, and the participation of Co as a synergistic catalytic site in the process while participating in the electron transfer cycle of Fe (II) and Fe(III). In addition, Co exhibited a significantly larger binding energy, which might involve the transfer of electrons, which in turn altered the electron cloud distribution and energy level structure of Co atoms, ultimately leading to an increase in the binding energy.

The stability of Fe<sub>4</sub>CoMOF after 7 days of storage was tested by determining its catalytic activity, and the results showed almost no decrease in catalytic activity compared to the initial catalytic activity (Fig. S3), indicating that Fe<sub>4</sub>CoMOF had good catalytic stability, which was attributed to the stability of its structure and composition.

**Table 1**  
The apparent Michaelis-Menten constant ( $K_m$ ) and maximum arrival velocity ( $V_{max}$ ) of Fe<sub>x</sub>CoMOFs with various proportions.

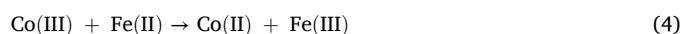
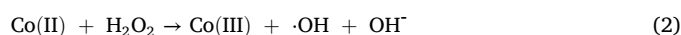
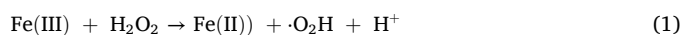
Catalyst	Substance	$K_m$ [mM]	$V_{max}$ [10 <sup>-7</sup> M·s <sup>-1</sup> ]
Fe <sub>5</sub> CoMOF	H <sub>2</sub> O <sub>2</sub>	1.89 ± 0.34	0.93 ± 0.04
	TMB	10.04 ± 1.43	0.97 ± 0.03
Fe <sub>4</sub> CoMOF	H <sub>2</sub> O <sub>2</sub>	1.78 ± 0.17	1.01 ± 0.06
	TMB	10.30 ± 1.62	0.73 ± 0.02
Fe <sub>3</sub> CoMOF	H <sub>2</sub> O <sub>2</sub>	1.81 ± 0.23	0.87 ± 0.04
	TMB	6.28 ± 0.98	0.84 ± 0.05

### 3.3. Mechanism investigation

To verify that the enhancement of POD-like activity of Fe<sub>x</sub>CoMOFs was related to the promotion of electron transfer between Fe species after Co doping, the electrocatalytic behavior of various material-modified electrodes was measured via CV before and after the addition of H<sub>2</sub>O<sub>2</sub>. In the blank electrolyte solution without H<sub>2</sub>O<sub>2</sub>, the REDOX peak currents corresponding to Fe(II) and Fe(III) on the Fe<sub>x</sub>CoMOF-modified electrodes were more significant than that on FeMOF, indicating that the addition of Co(II) promoted electron transfer between Fe (III) and Fe(II) (Inset in Fig. 3a). Enhanced reduction peak current corresponding to the reduction of Fe(III) to Fe(II) at -0.02 V was observed at the Fe<sub>x</sub>CoMOF-modified electrode after the addition of H<sub>2</sub>O<sub>2</sub>. This is consistent with several reported FeNi bimetallic MOF-modified electrodes exhibiting enhanced current in H<sub>2</sub>O<sub>2</sub> compared to monometallic MOFs (Mu et al., 2022; Shen et al., 2024), suggesting that the synergistic effect between the bimetallics as well as the electron transfer improved the electrocatalytic reduction of H<sub>2</sub>O<sub>2</sub>, which was further validated by the gradual increase of the reduction peak currents with increasing H<sub>2</sub>O<sub>2</sub> concentration (Fig. 3b). The above experimental data confirmed that Fe<sub>x</sub>CoMOF had electrocatalytic effect on the reduction of H<sub>2</sub>O<sub>2</sub>, and the order of current intensity was as follows: Fe<sub>4</sub>CoMOF > Fe<sub>3</sub>CoMOF > Fe<sub>5</sub>CoMOF > FeMOF, which was consistent with their POD-like activities. In the Fe<sub>4</sub>CoMOF systems, when the scanning rate increased gradually, the REDOX peak current also increased gradually (Fig. 3c), indicating that the electrocatalytic activity of Fe<sub>4</sub>CoMOF toward H<sub>2</sub>O<sub>2</sub> was also related to the scanning rate. In summary, Fe(III) in Fe<sub>x</sub>CoMOFs accepted electrons from the electrode surface to form Fe(II), which was then oxidized by H<sub>2</sub>O<sub>2</sub> to lose electrons to form Fe(III), and H<sub>2</sub>O<sub>2</sub> got electrons to be reduced to H<sub>2</sub>O. In this process, Co promoted the conversion of Fe(II) to Fe(III), thus amplifying the electrocatalysis.

ESR spectroscopy was used to study the generation of ·OH in various systems. A typical quadruple characteristic signal of 1:2:2:1 was observed in the Fe<sub>x</sub>CoMOFs and H<sub>2</sub>O<sub>2</sub> systems, demonstrating the production of ·OH and the highest amount in Fe<sub>4</sub>CoMOF (Fig. 3d). ESR could be employed to quantify the ·OH concentration produced by H<sub>2</sub>O<sub>2</sub> catalyzed by Fe<sub>4</sub>CoMOF. The intensity of the quadruple characteristic signal in the ESR spectra gradually increased with time (Fig. 3e), indicating that the amount of ·OH produced gradually increased, and the inset showed that the concentration of ·OH could reach 30 μmol/L when the catalysis was carried out for 10 min. To further confirm the production of ·OH, the characteristic fluorescence corresponding to 440 nm of TAOH was recorded (Fig. 3f). In the Fe<sub>4</sub>CoMOF system, the fluorescence signals were significantly enhanced.

Based on the above electrochemical experiments and ·OH verification experiments, electron transfer plays a key role in the POD-like activity of Fe<sub>x</sub>CoMOFs. Similar to previously reported results (Li et al., 2021c; Mu et al., 2022), Fe(III) reacted with H<sub>2</sub>O<sub>2</sub> to produce Fe(II) and ·O<sub>2</sub>H, and then Fe(II) reacted with H<sub>2</sub>O<sub>2</sub> to produce ·OH, while the addition of Co(II) promoted electron transfer between Fe(III) and Fe(II), thus producing more ·OH with enhanced POD-like activity and was closely related to the content of doped Co(II). Since Fe<sub>4</sub>CoMOF exhibited the best POD-like activity, Fe<sub>4</sub>CoMOF was selected for subsequent experiments. The equations for the catalytic mechanism are shown in Eqs. (1) to (4), which are a generalized catalytic mechanism in most reports on the enhancement of POD-like activity by bimetallic MOFs (Dang and Zhao, 2020; Jiang et al., 2024).



When antibacterial agents based on POD-like activity are used for

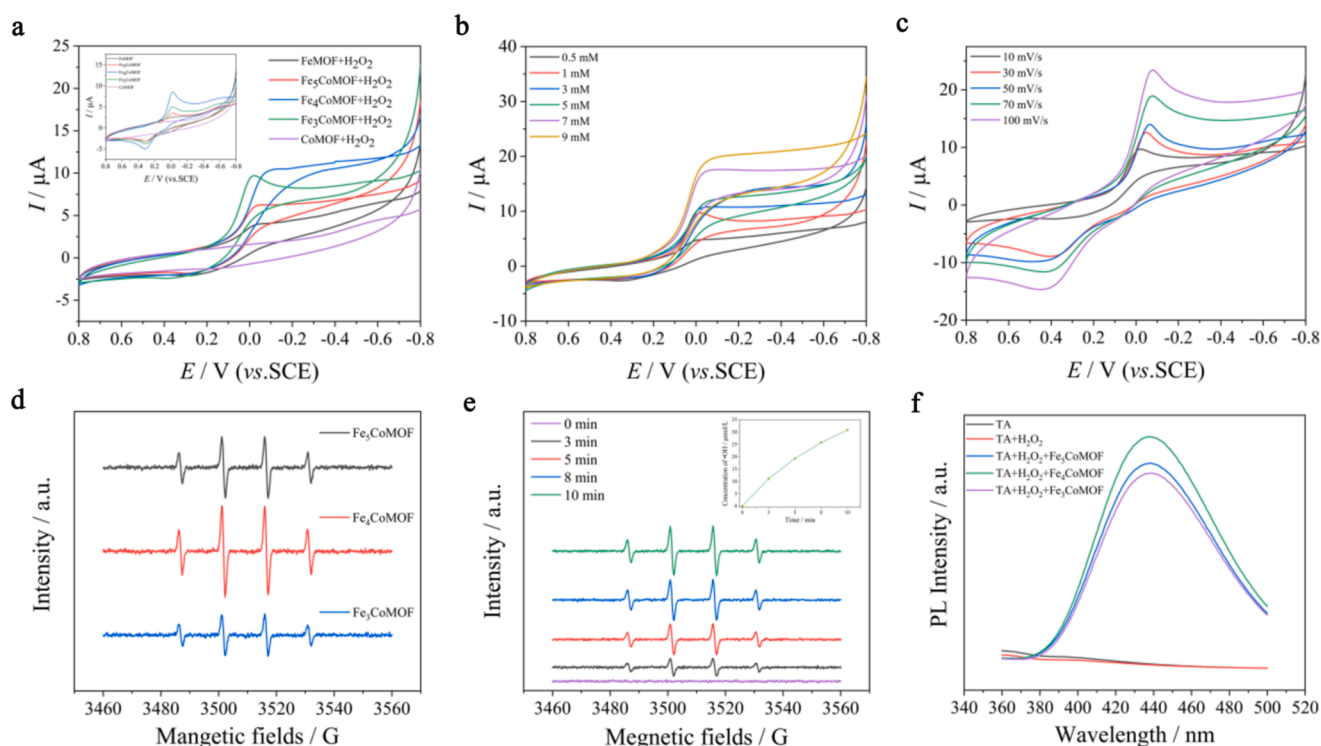


**Fig. 3.** (a) CV curves of FeMOF/GCE, Fe<sub>2</sub>CoMOF/GCE, Fe<sub>4</sub>CoMOF/GCE, Fe<sub>3</sub>CoMOF/GCE and CoMOF/GCE in N<sub>2</sub> saturated 0.1 M HAC-NaNC (pH 4.0) in the presence of 1 mM H<sub>2</sub>O<sub>2</sub> at a scan rate of 10 mV/s. Inset: CV curves of corresponding electrodes in solution without H<sub>2</sub>O<sub>2</sub>. (b) CV curves of Fe<sub>4</sub>CoMOF/GCE with different concentrations of H<sub>2</sub>O<sub>2</sub>. (c) CV curves of Fe<sub>4</sub>CoMOF/GCE with different scan rates. (d) ESR spectra of Fe<sub>x</sub>CoMOFs in the presence of H<sub>2</sub>O<sub>2</sub>. (e) ESR spectra of Fe<sub>4</sub>CoMOF in H<sub>2</sub>O<sub>2</sub> solution with time. Inset: Time dependence for concentration or yield of ·OH. (f) Fluorescence spectra of Fe<sub>x</sub>CoMOFs in the presence of H<sub>2</sub>O<sub>2</sub> and TA.

practical antibacterial applications, the presence of GSH in bacteria can significantly weaken the antibacterial effect by decreasing the ROS, so it is crucial for antibacterial agents to have the ability to deplete GSH (Qi et al., 2022). The ability of Fe<sub>4</sub>CoMOF to effectively scavenge GSH was investigated by the absorption peak at 412 nm of TNB<sup>·</sup> generated by the reaction of DTNB with GSH. As shown in Fig. S4, the absorbance at 412 nm decreased after the addition of Fe<sub>4</sub>CoMOF co-incubated with GSH, indicating a certain degree of GSH depletion, thus further enhancing the POD-like activity of Fe<sub>4</sub>CoMOF.

### 3.4. Establishment of the Fe<sub>4</sub>CoMOF/GOx cascade system

Surface adsorption is the most direct and simple method to immobilize natural enzymes directly on the surface of MOF through weak interactions such as van der Waals forces,  $\pi$ - $\pi$  interactions, hydrogen bonding and electrostatic interactions. Because of the non-specificity of the interaction between the enzyme and MOF, most MOFs can be used as carriers for immobilization of natural enzymes, which is not limited by the pore size or the presence or absence of specific functional groups on the MOF. A Fe<sub>4</sub>CoMOF/GOx cascade system was constructed by immobilizing GOx on Fe<sub>4</sub>CoMOF through physical interactions, and the interactions between Fe<sub>4</sub>CoMOF and GOx were investigated by Zeta potential measurements and XRD techniques. As can be seen in Fig. S5a, Fe<sub>4</sub>CoMOF itself was positively charged, and GOx was negatively charged because of the isoelectric point of GOx at 4.9, when GOx interacted with MOF it made the Zeta potential decreased, and with the amount of loaded GOx the Zeta potential decreased, indicating the adsorption of GOx on Fe<sub>4</sub>CoMOF. From Fig. S5b, it could be seen that after the adsorption of GOx on the Fe<sub>4</sub>CoMOF, some fine structures of the MOF in XRD pattern were covered by GOx and showed broad diffraction peaks, and only the diffraction peaks near 10.5° were still strong, and the intensity of the peaks decreased with the increase of the

GOx content.

The catalytic performance of Fe<sub>4</sub>CoMOF/GOx cascade reaction system in the presence of Glu was investigated. As shown in Fig. 4a, only when Glu coexisted with Fe<sub>4</sub>CoMOF/GOx, strong absorption peaks at 652 nm and color change were observed in the TMB solution, which indicated that the cascade catalysts based on Fe<sub>4</sub>CoMOF/GOx had been successfully prepared and were able to catalyze the production of H<sub>2</sub>O<sub>2</sub> from Glu. Methyl red appears in red color when the pH is less than 4.4, which can be used as pH indicator of cascade reaction to monitor the pH change caused by the production of gluconic acid. As shown in Fig. 4b, the colors of the control experiments were yellow, and only groups III and V changed significantly from yellow to red, indicating that the pH value decreased from 7.4 to below 4.4. These results confirmed that the production of gluconic acid during the cascade reaction lowered the pH of the system, which activated the POD-like activity of Fe<sub>4</sub>CoMOF and showed a significant absorbance. The activation of POD-like activity of Fe<sub>4</sub>CoMOF was associated with gluconic acid and H<sub>2</sub>O<sub>2</sub> production, thus it was necessary to optimize the conditions affecting the reaction of Glu and GOx. The cascade reaction system showed the highest catalytic activity in 0.5 mM PBS buffer (Fig. 4c). The absorbance of oxTMB gradually increased with increasing incubation time, reaching a maximum at 4 h (Fig. 4d). In addition, with the increase of Glu concentration, the absorbance of oxTMB continued to increase (Fig. 4e), indicating that more intermediate H<sub>2</sub>O<sub>2</sub> was produced by the cascade reaction, and at the same time, the production of gluconic acid activated the POD-like activity of Fe<sub>4</sub>CoMOF, resulting in the production of more ·OH. The effect of the amount of adsorbed GOx on the catalytic performance of the cascade system was explored, and when the mass ratio of Fe<sub>4</sub>CoMOF to GOx was varied from 1:0.05 to 1:5, the absorbance at 652 nm increased and then decreased, and reached a maximum at 1:0.5 (Fig. S6). This trend could be explained by the fact that an increase in GOx catalyzed the production of more H<sub>2</sub>O<sub>2</sub> from Glu, but an excess of

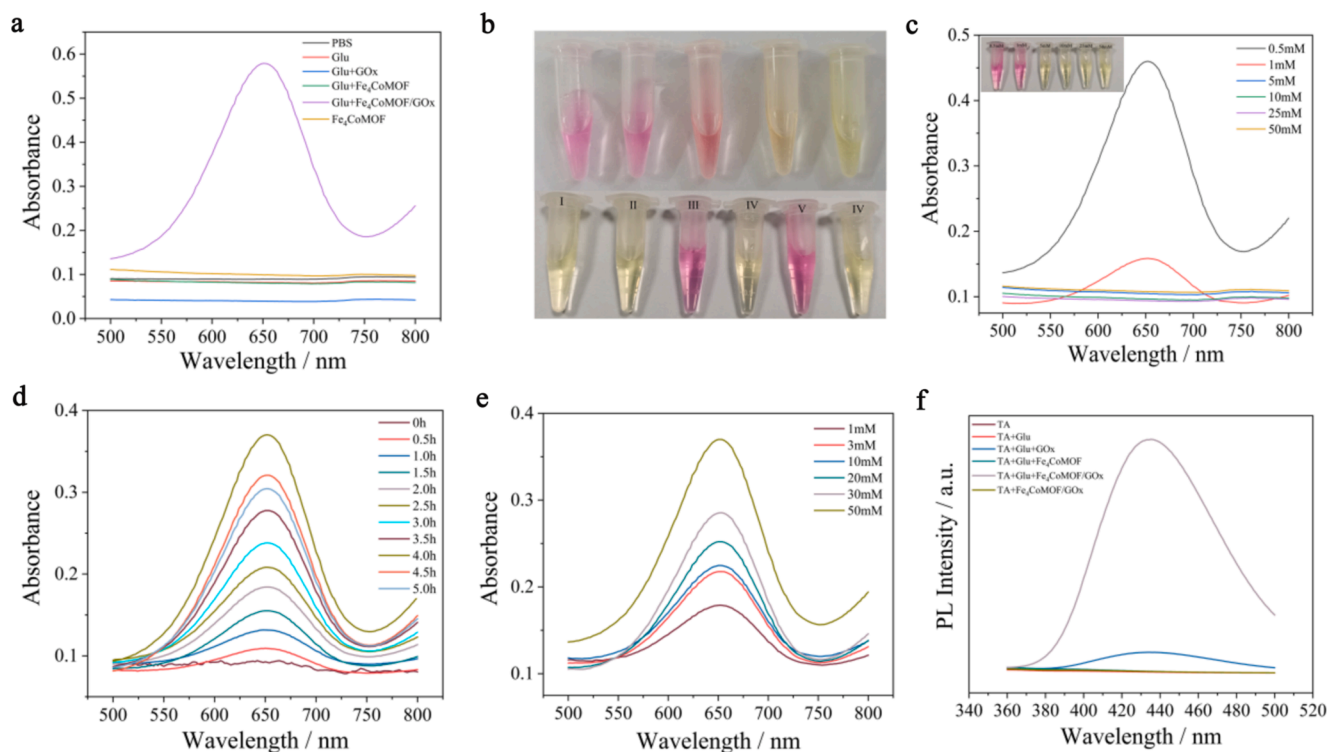


**Fig. 4.** (a) UV-vis spectra of various reaction systems in the presence of TMB. (b) Photos of HAC-NaAc buffers at different pH (3, 4, 5, 6, and 7) with the addition of methyl red and various reaction systems in the presence of methyl red after 4 h incubation. (c) UV-vis spectra of group V incubated in PBS buffer with various concentrations. (d) Time-dependent absorbance changes in  $\text{Fe}_4\text{CoMOF}/\text{GOx} + \text{Glu}$  system. (e) UV-vis spectra of various concentrations of Glu incubated with  $\text{Fe}_4\text{CoMOF}/\text{GOx}$ . (f) Fluorescence spectra of various reaction systems in PBS buffer after 12 h reaction.

GOx also masked some of the catalytic sites of  $\text{Fe}_4\text{CoMOF}$ . TA fluorescence experiments also confirmed the successful construction of cascade system (Fig. 4f). The successful establishment of the  $\text{Fe}_4\text{CoMOF}/\text{GOx}$  nanocatalyst could maintain high catalytic activity under normal

physiological conditions and catalyze nontoxic Glu to produce toxic  $\cdot\text{OH}$ , which is conducive to the application of MOFs to biological anti-bacterial agents without the addition of exogenous  $\text{H}_2\text{O}_2$ .

The stability of  $\text{Fe}_4\text{CoMOF}/\text{GOx}$  nanocomposites in PBS was tested

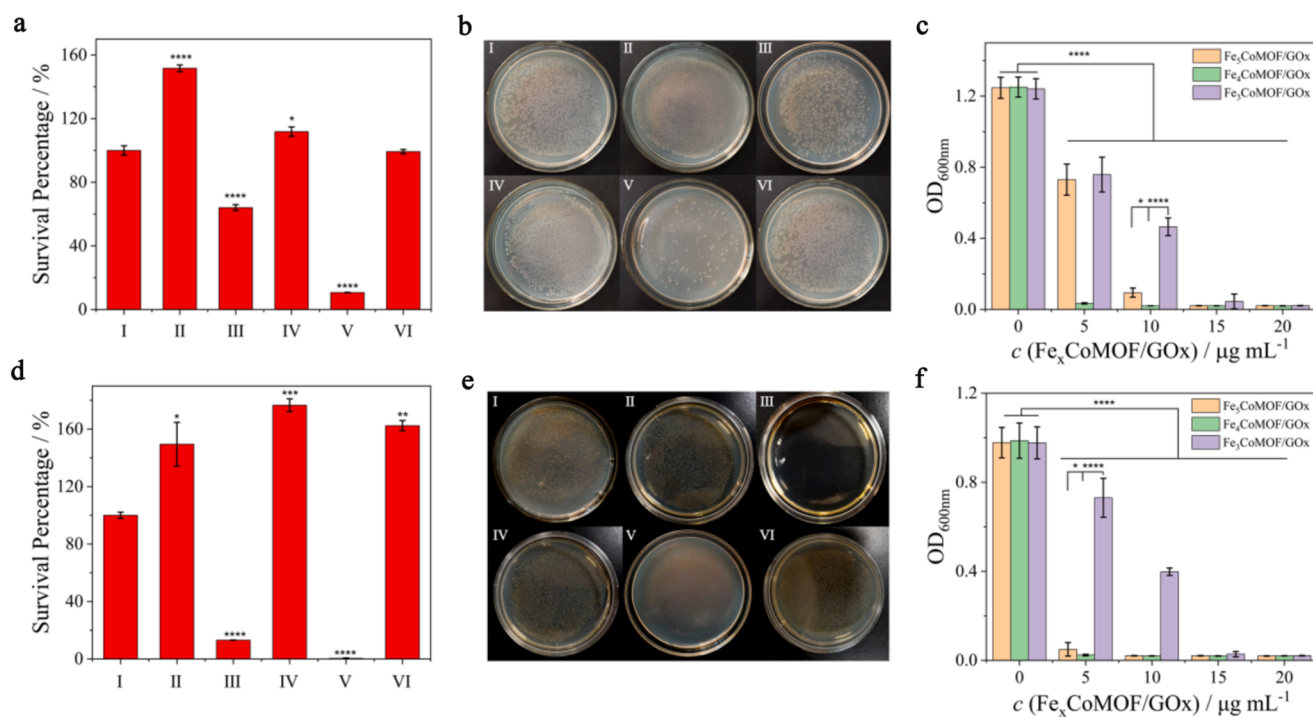


**Fig. 5.** The survival rate of (a) *E. coli* and (d) *S. aureus* treated with various treatments and solid agar plate photographs for (b) *E. coli* and (e) *S. aureus* treated with various treatments. The  $\text{OD}_{600\text{nm}}$  of (c) *E. coli* and (f) *S. aureus* liquid medium incubated with various concentrations of  $\text{Fe}_x\text{CoMOF}/\text{GOx}$  with the addition of Glu.

for 7 days, and the results were shown in Fig. S7, the catalytic performance of Fe<sub>4</sub>CoMOF/GOx on Glu decreased by 12 % after 7 days, which indicated that it had good stability in PBS. The small change in Zeta potential of Fe<sub>4</sub>CoMOF/GOx after catalyzing Glu also further indicated that MOF could serve as an excellent carrier for GOx, ensuring its effectiveness as a biocatalyst carrier (Inset of Fig. S5a).

### 3.5. In vitro antibacterial performance

The antibacterial activity of Fe<sub>4</sub>CoMOF/GOx with Glu was evaluated using the typical gram-negative bacteria *E. coli* and gram-positive bacteria *S. aureus*. OD<sub>600nm</sub> value was used to evaluate the influence of various treatments on bacteria. As shown in Fig. 5a and 5d, when the bacterial survival rate of the PBS treatment group was 100 %, the survival rates of the group II and IV increased owing to the influence of Glu and those of the VI group remained unchanged. Only the survival rates of group III and V were reduced. Group III showed antibacterial effect owing to the production of H<sub>2</sub>O<sub>2</sub> by the reaction of Glu and GOx. However, the antibacterial activity was limited. The group V showed the highest antibacterial effect owing to the production of abundant ·OH, which reduced the survival rate of *E. coli* to 10 %, and almost all *S. aureus* were inactivated. Similar results were obtained for the various treatment groups using the plate counting method (Fig. 5b and 5e).

MIC is the minimum concentration of an antibacterial agent required for the complete inhibition of bacterial growth, which is an important index for measuring the antibacterial effect. The lower the MIC value, the stronger the antibacterial effect of the antibacterial agent. As shown in Fig. 5c and 5f, the liquid medium containing Fe<sub>4</sub>CoMOF/GOx and Glu inhibited the growth of bacteria when the concentrations of Fe<sub>4</sub>CoMOF/GOx exceeded 10 μg mL<sup>-1</sup> and 5 μg mL<sup>-1</sup>, respectively. These results showed that the MIC values of Fe<sub>4</sub>CoMOF/GOx against *E. coli* and *S. aureus* were 10 μg mL<sup>-1</sup> and 5 μg mL<sup>-1</sup>, respectively, indicating that Fe<sub>4</sub>CoMOF/GOx had an excellent bactericidal effect against high concentrations of bacteria at low doses, which could effectively reduce the antibacterial agent usage and would have an advantage in improving the biosafety when compared to literature reports (Table 2).

The effect of pH changes during Glu activation on bacterial survival was further investigated. During the activation of Glu, the gluconic acid produced with the reaction time of Glu with GOx caused the pH of the system to gradually decrease from the initial neutral to 3–4, as evidenced by the gradual change of color from yellow to red in the presence of methyl red indicator (Fig. S8b). Therefore, to investigate the effect of

**Table 2**

Comparisons of dosages and inactivation rates of the Fe<sub>4</sub>CoMOF/GOx with other antibacterial materials.

Materials	Bacteria (CFU mL <sup>-1</sup> )	Dosage (μg mL <sup>-1</sup> )	Inactivation rate (%)	Ref.
2D MOF/GOx	10 <sup>6</sup>	100	90 % for <i>E. coli</i> 96 % for <i>S. aureus</i>	Liu et al., 2019
ZIF8/Au-GOx	10 <sup>6</sup>	8 4	91.17 % for <i>E. coli</i> 100 % for <i>S. aureus</i>	Wang et al., 2022b
GOx@Fe-GMP CPN	10 <sup>7</sup>	10	99 % for <i>E. coli</i> 99 % for <i>S. aureus</i>	Zhao et al., 2021a
GFeF	10 <sup>8</sup>	100	91.17 % for <i>E. coli</i> 100 % for <i>S. aureus</i>	Li et al., 2021a
Mg/EGCG	10 <sup>5</sup>	20	80 % for <i>S. aureus</i>	Hu et al., 2019
Fe <sub>4</sub> CoMOFs/GOx	10 <sup>8</sup>	10 5	90 % for <i>E. coli</i> 100 % for <i>S. aureus</i>	This work

pH change on bacterial survival during the reaction process, we investigated the effect of different reaction times on the antibacterial activity of the Fe<sub>4</sub>CoMOF/GOx + Glu cascade system, which could be seen from Fig. S8a and Fig. S8c. Although a slight decrease in pH had been observed at 1 h and 2 h, it was not sufficient to activate the POD-like activity of Fe<sub>4</sub>CoMOF, and at the same time sufficient Glu in the system promoted the bacterial propagation; after 3 h, the bacterial survival rate was significantly reduced, and the increase in antibacterial activity was caused by the activation of Fe<sub>4</sub>CoMOF by decreasing the pH from 7.4 to about 4.4, which produced enhanced ·OH. Therefore, the decrease in pH enhanced the antibacterial effect of Fe<sub>4</sub>CoMOF.

The live and dead bacteria were stained with Calcein-AM and PI, respectively. As shown in Fig. 6, most *E. coli* and *S. aureus* survived in groups I, II, IV, and VI, while green and red fluorescence signals were observed in group III. In contrast, group V showed a broad red fluorescence signal, indicating severe damage to the plasma membranes of *E. coli* and *S. aureus*. The effect of each treatment group on intracellular ROS production was investigated using DCFH-DA as a ROS probe. As shown in Fig. 6, there was almost no ROS production in groups I, II, IV, and VI. The green fluorescence that could be observed in group III was due to the production of H<sub>2</sub>O<sub>2</sub> from GOx-catalyzed Glu, whereas a strong green fluorescence could be clearly observed in group V, indicating that the Fe<sub>4</sub>CoMOF/GOx cascade system was able to greatly enhance the production of intracellular ROS in the bacterial cells. The morphologies of *E. coli* and *S. aureus* were further characterized before and after treatment with Fe<sub>4</sub>CoMOF/GOx using SEM (Fig. 6). In the control group, *E. coli* and *S. aureus* showed typical rod-like and globular morphology, respectively, with smooth surfaces and integral cell walls. Simultaneously, the toxic ·OH produced after Fe<sub>4</sub>CoMOF/GOx treatment disrupted the morphology of bacterial cells to a certain extent, and the cell walls became rough and compressed. Consequently, Fe<sub>4</sub>CoMOF/GOx produced a large number of ·OH through the cascade reaction to damage the bacteria and exhibited an excellent bactericidal performance.

The biocompatibility of nanozymes is a prerequisite for evaluating the feasibility of their application. The effects of various concentrations of Fe<sub>4</sub>CoMOF on Mouse fibroblast L929 cells were determined using the CCK-8 assay. The cell without Fe<sub>4</sub>CoMOF treatment served as the blank control group, and the survival rate was defined as 100 %. After incubation with various concentrations of Fe<sub>4</sub>CoMOF for 24 h, the viability of cells did not decrease significantly even when the highest concentration of 50 μg mL<sup>-1</sup> used (Fig. S9); this indicated that the prepared Fe<sub>4</sub>CoMOF had low cytotoxicity and good biocompatibility.

### 3.6. In vivo antibacterial performance

Bacterial infection of the wound itself is one of the main factors that hinder wound healing. The effect of Fe<sub>4</sub>CoMOF/GOx based cascade system on wound healing was evaluated. As shown in Fig. 7a, the healing rate of group V was fastest among all the groups. The wound healed almost entirely after eight days, which demonstrated that the Fe<sub>4</sub>CoMOF/GOx-catalyzed cascade reaction for producing toxic ·OH could be applied to the wound surface to inhibit *E. coli* and thus accelerate wound healing. The wounds in groups II, III and IV exhibited worse healing effects compared to those in group I, which can be explained by the fact that Glu can provide nutrients for the reproduction of *E. coli* and hinder the elimination of *E. coli*. The *in vivo* antibacterial effect of the Fe<sub>4</sub>CoMOF/GOx cascade system was further evaluated. Bacteria were collected from the wound tissue on day 7, dispersed in saline to obtain bacterial suspensions, and cultured to determine the number of bacteria by plate counting method. As shown in Fig. 7b and Fig. 7c, *S. aureus* and *E. coli* colonies were almost completely eliminated from the wound tissues treated in group V. This indicated that the Fe<sub>4</sub>CoMOF/GOx cascade system had a good antimicrobial effect *in vivo*, which is conducive to accelerating wound healing. In addition, compared with those in blank control group, there were no significant differences in the weight changes in the other groups of mice (Fig. 7d), indicating that all

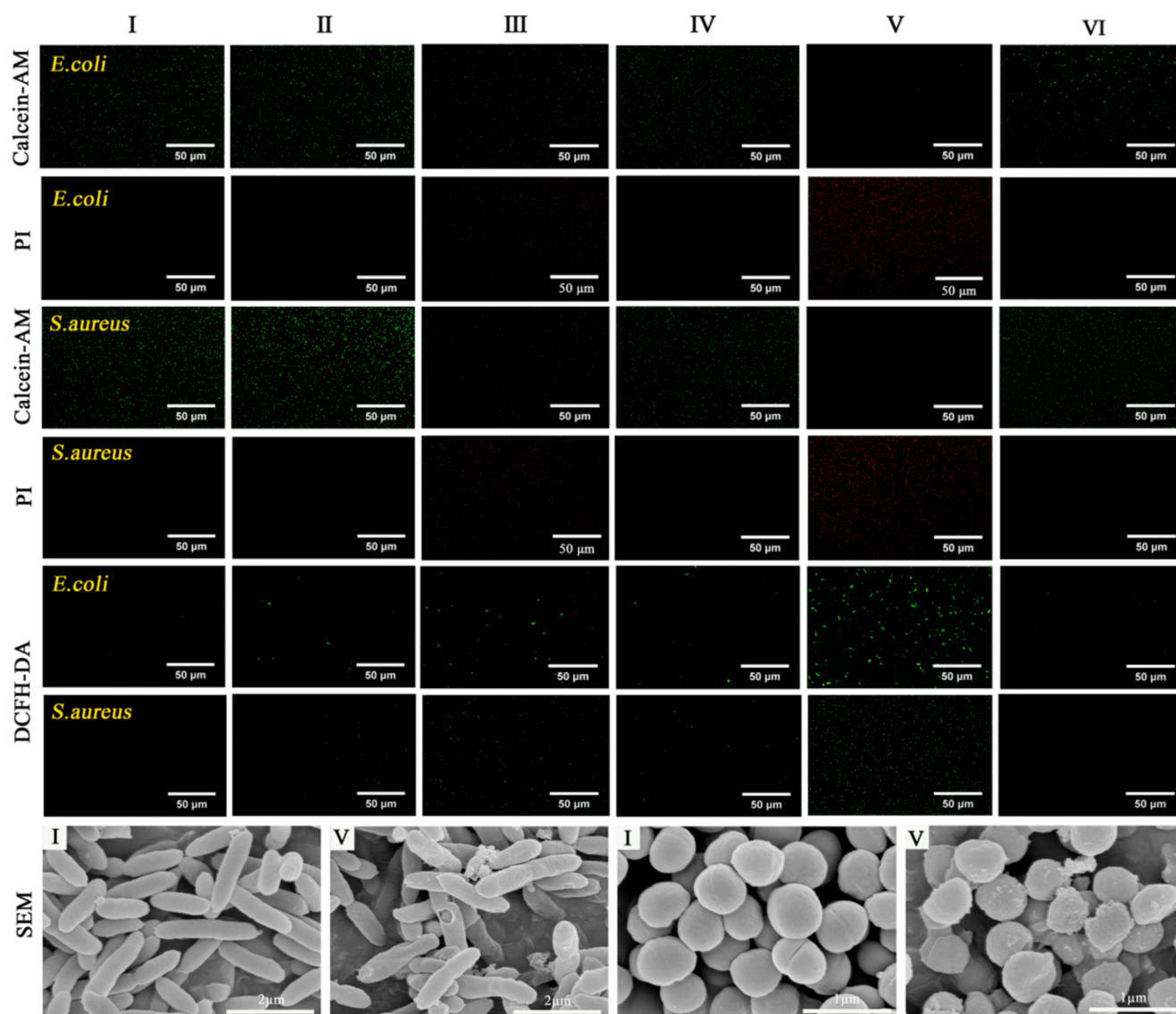


**Fig. 6.** Fluorescence microscopy images of Calcein-AM/PI bacterial live/dead staining and DCFH-DA staining and SEM images for *E. coli* and *S. aureus* treated with various systems.

treatments had no significant effects on the average growth of mice. To further evaluate the wound healing in each treatment group, wound tissues were collected eight days later for H&E staining and immunohistochemical staining analyses to provide more reliable details (Fig. 7e and Fig. 7f). Group V had a good skin structure and fewer capillaries, which indicated that the wound site was almost completely regenerated. The expression of pro-inflammatory cytokines IL-6 and TNF- $\alpha$  in wound skin tissues was quantitatively analyzed (Fig. S10), and the two pro-inflammatory factors were significantly down-regulated in the skin tissues of group IV relative to those of group I, which reduced inflammatory responses, facilitated epithelial tissue regeneration and promoted wound healing. Therefore, Fe<sub>4</sub>CoMOF/GOx promoted wound healing by exerting an excellent antibacterial effect.

#### 4. Conclusions

Several Fe<sub>x</sub>CoMOFs were successfully synthesized, and various bimetallic proportions resulted in various sizes, specific surface areas, surface defects, and morphologies. Moreover, the doping of Co(II) promoted the electron transfer of Fe(III) and Fe(II), thus enhancing the POD-like activity. Among all systems, Fe<sub>4</sub>CoMOF had the most

considerable POD-like activity. Owing to the large surface area, high porosity, and significant enzyme-like activity of the Fe<sub>4</sub>CoMOF, an enzyme cascade reaction system for the adsorption of GOx was constructed. The system produced the POD-like substrate H<sub>2</sub>O<sub>2</sub> in situ in the presence of Glu. In addition, the gluconic acid generated provided an acidic environment required for a high enzyme-like activity. Therefore, enzyme-like activity was significantly enhanced and inhibited *E. coli* and *S. aureus* growth effectively. This system exhibited high biocompatibility and bio-safety. In a bacterial infection wound model, Fe<sub>4</sub>CoMOF/GOx significantly exerted antibacterial effects and promoted wound healing. This study will promote research on MOFs-based nanozyme activity regulation and cascade systems, accelerate the development of nanozyme-catalyzed antibacterial therapy and expand the applications of nanozyme in biocatalytic and biomedicine.

#### CRediT authorship contribution statement

**Siyuan Zhang:** Writing – original draft, Validation, Methodology, Investigation, Formal analysis, Data curation. **Wenbo Wu:** Writing – original draft, Visualization, Validation, Methodology, Investigation. **Ya Li:** Investigation, Formal analysis, Data curation. **Dongxin Wang:**

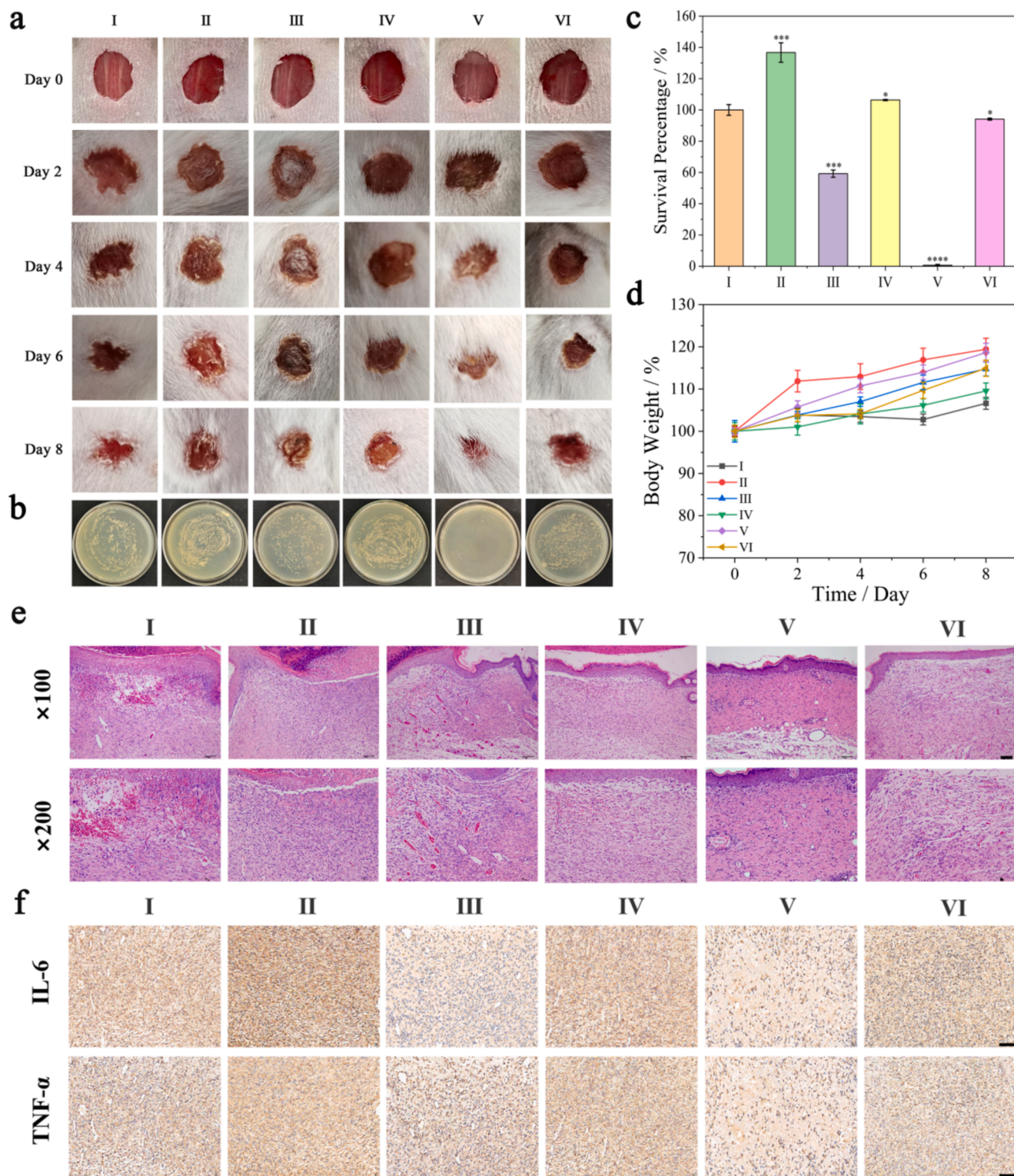


**Fig. 7.** (a) Photographs of *E. coli*-infected wounds of mice after various treatments on day 0, day 2, day 4, day 6, and day 8. (b) Photographs of bacterial colonies obtained from wound tissue. (c) Quantitative analysis of surviving bacteria in wound. (d) Bodyweight of mice during varied treatments. (e) Images of H&E-stained skin samples dissected from mice for histopathological analysis. Scale bar:  $\times 100$ : 100  $\mu\text{m}$ ;  $\times 200$ : 10  $\mu\text{m}$ . (f) Immunohistochemical staining of pro-inflammatory factor IL-6, TNF- $\alpha$  in different groups on the day 8. Scale bar: 100  $\mu\text{m}$ .

Visualization, Data curation. **Xiangjun Li**: Writing – review & editing, Supervision, Resources. **Jisheng Nie**: Writing – review & editing, Resources. **Hong Cui**: Writing – review & editing, Supervision, Resources, Project administration, Funding acquisition, Conceptualization.

#### Acknowledgements

This work was supported by the National Natural Science Foundation of China (82120108016), the Natural Science Foundation of Shanxi Province (202203021211233), and the Science and Technology

Innovation Project of Higher Education in Shanxi Province (2020L0190). This work was also supported by the MOE Key Laboratory of Coal Environmental Pathogenicity and Prevention, Shanxi Medical University.

## Appendix A. Supplementary data

Supplementary data to this article can be found online at <https://doi.org/10.1016/j.arabjc.2024.106032>.

## References

- Alavijeh, R.K., Beheshti, S., Akhbari, K., et al., 2018. Investigation of reasons for metal-organic framework's antibacterial activities. *Polyhedron*. 156, 257–278. <https://doi.org/10.1016/j.poly.2018.09.028>.
- Chen, Z.W., Wang, Z.Z., Ren, J.S., et al., 2018. Enzyme mimicry for combating bacteria and biofilms. *Acc. Chem. Res.* 51, 789–799. <https://doi.org/10.1021/acs.accounts.8b00011>.
- Chen, L.Y., Wang, H.F., Li, C.X., et al., 2020. Bimetallic metal-organic frameworks and their derivatives. *Chem. Sci.* 11, 5369–5403. <https://doi.org/10.1039/D0SC01432J>.
- Dang, X.M., Zhao, H.M., 2020. Bimetallic Fe/Mn metal-organic-frameworks and Au nanoparticles anchored carbon nanotubes as a peroxidase-like detection platform with increased active sites and enhanced electron transfer. *Talanta*. 201, 120678. <https://doi.org/10.1016/j.talanta.2019.120678>.
- Hu, C., Zhang, F.J., Kong, Q.S., Lu, Y.H., Zhang, B., Wu, C., Luo, R.F., Wang, Y.B., 2019. Synergistic chemical and photodynamic antimicrobial therapy for enhanced wound healing mediated by multifunctional light-responsive nanoparticles. *Biomacromolecules* 20, 4581–4592. <https://doi.org/10.1021/acs.biomac.9b01401>.
- Huang, Y.Y., Ren, J.S., Qu, X.G., 2019. Nanozymes: classification, catalytic mechanisms, activity regulation, and applications. *Chem. Rev.* 119, 4357–4412. <https://doi.org/10.1021/acs.chemrev.8b00672>.
- Huang, L.J., Sun, D.W., Pu, H.B., 2022. Photosensitized peroxidase mimicry at the hierarchical 0D/2D heterojunction-like quasi metal-organic framework interface for boosting biocatalytic disinfection. *Small*. 18, 2200178. <https://doi.org/10.1002/sml.202200178>.
- Jiang, M.Q., Xu, Z.X., Li, L.J., et al., 2024. Fe/Cu MOFs of Fe<sup>2+</sup>-rich and Cu-doping via in situ reduction as nanozyme for peroxidase-like catalytic enhancement. *Microchim. Acta*. 191, 478. <https://doi.org/10.1007/s00604-024-06562-3>.
- Jones, K., Patel, N., Levy, M., et al., 2008. Global trends in emerging infectious diseases. *Nature*. 451, 990–993. <https://doi.org/10.1038/nature06536>.
- Kong, Q.D., Yang, Y.S., 2021. Recent advances in antibacterial agents. *Bioorg. Med. Chem. Lett.* 35, 127799. <https://doi.org/10.1016/j.bmcl.2021.127799>.
- Koo, H., Allan, R., Howlin, R., et al., 2017. Targeting microbial biofilms: current and prospective therapeutic strategies. *Nat. Rev. Microbiol.* 15, 740–755. <https://doi.org/10.1038/nrmicro.2017.99>.
- Li, T., Qiu, H.Q., Liu, N., et al., 2020. Construction of self-activated cascade metal-organic framework/enzyme hybrid nanoreactors as antibacterial agents construction of self-activated cascade metal hybrid nanoreactors as antibacterial agents. *Colloid Surface B*. 191, 111001. <https://doi.org/10.1016/j.colsurfb.2020.111001>.
- Li, Y.T., Wang, L., Liu, H., et al., 2021a. Ionic Covalent-organic framework nanozyme as effective cascade catalyst against bacterial wound infection. *Small*. 17, 2100756. <https://doi.org/10.1002/sml.202100756>.
- Li, J., Zhao, J., Li, S.Q., et al., 2021c. Synergistic effect enhances the peroxidase-like activity in platinum nanoparticle-supported metal-organic framework hybrid nanozymes for ultrasensitive detection of glucose. *Nano Res.* 14, 4689–4695. <https://doi.org/10.1007/s12274-021-3406-z>.
- Li, Y.Y., Zhu, W.X., Li, J.S., et al., 2021b. Research progress in nanozyme-based composite materials for fighting against bacteria and biofilms. *Colloid Surface B*. 198, 111465. <https://doi.org/10.1016/j.colsurfb.2020.111465>.
- Liang, H., Liu, R.P., Hu, C.Z., et al., 2021. Synergistic effect of dual sites on bimetal-organic frameworks for highly efficient peroxide activation. *J. Hazard. Mater.* 406, 124692. <https://doi.org/10.1016/j.jhazmat.2020.124692>.
- Liu, X.P., Yan, Z.Q., Zhang, Y., et al., 2019. Two-dimensional metal-organic framework/enzyme hybrid nanocatalyst as a benign and self-activated cascade reagent for *in vivo* wound healing. *ACS Nano*. 13, 5222–5230. <https://doi.org/10.1021/acsnano.8b09501>.
- Ma, B.J., Wang, S., Liu, F., et al., 2019. Self-assembled copper-amino acid nanoparticles for in situ glutathione “AND” H<sub>2</sub>O<sub>2</sub> sequentially triggered chemodynamic therapy. *J. Am. Chem. Soc.* 141, 849–857. <https://doi.org/10.1021/jacs.8b08714>.
- Maleki, A., Shahbazi, M.A., Alinezhad, V., et al., 2020. The progress and prospect of zeolitic imidazolate frameworks in cancer therapy, antibacterial activity, and biomineralization. *Adv. Healthc. Mater.* 9, 2000248. <https://doi.org/10.1002/adhm.202000248>.
- Matlock, A., Garcia, J.A., Moussavi, K., et al., 2021. Advances in novel antibiotics to treat multidrug-resistant gram-negative bacterial infections. *Intern. Emerg. Med.* 16, 2231–2241. <https://doi.org/10.1007/s11739-021-02749-1>.
- Mei, L.Q., Zhu, S., Liu, Y.P., et al., 2021. An overview of the use of nanozymes in antibacterial applications. *Chem. Eng. J.* 418, 129431. <https://doi.org/10.1016/j.cej.2021.129431>.
- Mu, Z., Wu, S., Guo, J.J., et al., 2022. Dual mechanism enhanced peroxidase-like activity of Iron-nickel bimetal-organic framework nanozyme and its application for biosensing. *ACS Sustainable Chem. Eng.* 10, 2984–2993. <https://doi.org/10.1021/acscuschemeng.1c07975>.
- Qi, Y., Ren, S.S., Ye, J.W., et al., 2022. Infection microenvironment-activated core-shell nanoassemblies for photothermal/chemodynamic synergistic wound therapy and multimodal imaging. *Acta Biomater.* 143, 445–458. <https://doi.org/10.1016/j.actbio.2022.02.034>.
- Reddy, A.J.M., Babua, M.S.S., Nagaraju, P., 2022. ZnNi(NA) (NA= Nicotinic acid) bimetallic mesoporous MOFs as a sensing platform for ethanol, formaldehyde and ammonia at room temperature. *Solid State Sci.* 125, 106819. <https://doi.org/10.1016/j.solidstatesciences.2022.106819>.
- Shen, H., Tang, Y., Ma, H.M., 2024. Accelerated peroxidase-like activity of ultrathin amine-tagged bimetallic MOF-74 nanozyme for construction of versatile bioassays from small molecules to enzymes and bacteria. *Microchem. J.* 201, 110706. <https://doi.org/10.1016/j.microc.2024.110706>.
- Shi, Q.Y., Zhao, Y., Liu, M.H., et al., 2023. Engineering platelet membrane-coated bimetallic MOFs as biodegradable nanozymes for efficient antibacterial therapy. *Small* 2309366. <https://doi.org/10.1002/sml.202309366>.
- Tian, M., Zhou, L.P., Fan, C., et al., 2023. Bimetal-organic framework/GOx-based hydrogel dressings with antibacterial and inflammatory modulation for wound healing. *Acta Biomater.* 158, 252–265. <https://doi.org/10.1016/j.actbio.2022.12.049>.
- Wang, D.K., Huang, R.K., Liu, W.J., et al., 2014. Fe-based MOFs for photocatalytic CO<sub>2</sub> reduction: role of coordination unsaturated sites and dual excitation pathways. *ACS Catal.* 4, 4254–4260. <https://doi.org/10.1021/cs501169t>.
- Wang, J., Liu, C., Feng, J.Y., et al., 2020. MOFs derived Co/Cu bimetallic nanoparticles embedded in graphitized carbon nanocubes as efficient Fenton catalysts. *J. Hazard. Mater.* 394, 122567. <https://doi.org/10.1016/j.jhazmat.2020.122567>.
- Wang, H.H., Yu, S.W., Meng, X.G., et al., 2022a. Facile synthesis of fumarate-type iron-cobalt bimetallic MOFs and its application in photo-Fenton degradation of organic dyes. *J. Solid State Chem.* 314, 123431. <https://doi.org/10.1016/j.jssc.2022.123431>.
- Wang, M.X., Zhou, X., Li, Y.H., et al., 2022b. Triple-synergistic MOF-nanozyme for efficient antibacterial treatment. *Bioact. Mater.* 17, 289–299. <https://doi.org/10.1016/j.bioactmat.2022.01.036>.
- Wen, J.F., Liu, X., Liu, L.N., et al., 2021. Bimetal cobalt-Iron based organic frameworks for coordinated sites as synergistic catalyst for Fenton catalysis study and antibacterial efficiency. *Colloid Surface a*. 610, 125683. <https://doi.org/10.1016/j.colsurfa.2020.125683>.
- Wu, X.L., Ge, J., Yang, C., et al., 2015. Facile synthesis of multiple enzyme-containing metal-organic frameworks in a biomolecule-friendly environment. *Chem. Commun.* 51, 13408–13411. <https://doi.org/10.1039/C5CC05136C>.
- Wu, Q.S., Yang, H.P., Kang, L., et al., 2020. Fe-based metal-organic frameworks as Fenton-like catalysts for highly efficient degradation of tetracycline hydrochloride over a wide pH range: Acceleration of Fe(II)/Fe(III) cycle under visible light irradiation. *Appl. Catal. B-Environ.* 263, 118282. <https://doi.org/10.1016/j.apcatb.2019.118282>.
- Xi, J.Q., Wei, G., An, L.F., et al., 2019. Copper/carbon hybrid nanozyme: tuning catalytic activity by copper state for antibacterial therapy. *Nano Lett.* 19, 7645–7654. <https://doi.org/10.1021/acs.nanolett.9b02242>.
- Xiong, X.Q., Huang, Y.Y., Lin, C.X., et al., 2019. Recent advances in nanoparticulate biomimetic catalysts for combating bacteria and biofilms. *Nanoscale*. 11, 22206–22215. <https://doi.org/10.1039/C9NR05054J>.
- Yang, D.Z., Chen, Z.Z., Gao, Z., et al., 2020. Nanozymes used for antimicrobials and their applications. *Colloid Surface B*. 195, 111252. <https://doi.org/10.1016/j.colsurfb.2020.111252>.
- Yang, L.X., Yang, H.Q., Yin, S.Y., et al., 2022. Fe single-atom catalyst for efficient and rapid Fenton-like degradation of organics and disinfection against bacteria. *Small*. 18, 2104941. <https://doi.org/10.1002/sml.202104941>.
- Ye, L., Cao, Z., Liu, X.M., et al., 2022. Noble metal-based nanomaterials as antibacterial agents. *J. Alloy. Compd.* 904, 164091. <https://doi.org/10.1016/j.jallcom.2022.164091>.
- Zhang, Y.N., Jin, Y.L., Cui, H.X., et al., 2020. Nanozyme-Based Catalytic Theranostics. *RSC Adv.* 10, 10–20. <https://doi.org/10.1039/C9RA09021E>.
- Zhang, C.Y., Yan, L., Wang, X., et al., 2019. Tumor microenvironment-responsive Cu<sub>2</sub>(OH)PO<sub>4</sub> nanocrystals for selective and controllable radiosensitization via the X-ray-triggered Fenton-like reaction. *Nano Lett.* 19, 1749–1757. <https://doi.org/10.1021/acs.nanolett.8b04763>.
- Zhao, J.H., Bao, X.F., Meng, T., et al., 2021a. Fe (II)-driven self-assembly of enzyme-like coordination polymer nanoparticles for cascade catalysis and wound disinfection applications. *Chem. Eng. J.* 420, 129674. <https://doi.org/10.1016/j.cej.2021.129674>.
- Zhao, X.P., Zhang, N., Yang, T.T., et al., 2021b. Bimetallic metal-organic frameworks: enhanced peroxidase-like activities for the self-activated cascade reaction. *ACS Appl. Mater. Interfaces*. 13, 36106–36116. <https://doi.org/10.1021/acsmi.1c05615>.